



Cite this: *CrystEngComm*, 2016, 18, 8472

## Crystal structure and phase transitions of a layered perovskite-like CsScF<sub>4</sub> crystal†

A. S. Krylov,<sup>\*a</sup> M. S. Molokeev,<sup>ab</sup> S. V. Misyul,<sup>c</sup> S. N. Krylova,<sup>a</sup> A. S. Oreshonkov,<sup>ac</sup> A. A. Ivanenko,<sup>a</sup> V. A. Zykova,<sup>d</sup> Y. N. Ivanov,<sup>a</sup> A. A. Sukhovskiy,<sup>a</sup> V. N. Voronov,<sup>a</sup> I. N. Safonov<sup>c</sup> and A. N. Vtyurin<sup>ac</sup>

This work is devoted to the complex research on temperature phase transitions in a CsScF<sub>4</sub> crystal. The crystal structure was solved and refined at different temperatures by using the Rietveld method. Structural phase transitions were investigated by using the following spectroscopic methods, some of them for the first time: Brillouin spectroscopy, Raman spectroscopy, IR absorption spectroscopy and NMR. The symmetry analysis of the Brillouin zone center of all phases is presented. The vibrational spectra of the crystal in three phases have been calculated. The structural phase transition mechanism was determined. The transitions at  $T_1 = 475$  K and  $T_2 = 317.5$  K are of displacement type. The Raman soft modes have been associated with rotations of the ScF<sub>6</sub> octahedral group.

Received 17th May 2016,  
Accepted 5th September 2016

DOI: 10.1039/c6ce01144f

www.rsc.org/crystengcomm

## 1 Introduction

The crystals whose high symmetry phase belongs to the space group  $D_{4h}^{1h}$ - $P4/mmm$  have been under intense scrutiny in recent few years. Among them, the layered perovskite-like compounds with a  $TlAlF_4$ -type structure are remarkable for retaining the infinite chains of vortex-sharing octahedra as an essential feature of the perovskite structure. Several compounds of the series exhibit phase transitions (PT) to a superconductive state, for example,  $Tl$ - $Ca$ - $Ba$ - $Cu$ - $O$  compounds containing constituents with a high-temperature superconductive phase.<sup>1,2</sup>

$ABX_4$  crystals with a  $TlAlF_4$ -type structure are known to have compounds where the A position is taken by zigzag polyethylene diammonium ions ( $[NH_3(CH_2)_nNH_3]^+$ ), essentially increasing the distances between the layers of connected octahedral groups  $BX_6$ .<sup>3</sup> The structure of such compounds was studied<sup>3</sup> for chlorides with  $B = Mn, Cd, Cu$  and  $n = 2-5$ . Many of the mentioned compounds have sequences of phase transitions (see ref. 1 and 4–6). Earlier phase transitions in crystals of the  $MAF_4$  family ( $M = Tl, K, Rb, NH_4$ ) were studied by various techniques (Brillouin and ultrasonic,<sup>7,8</sup> Raman,<sup>9,10</sup> Raman under high hydrostatic pres-

sure,<sup>11,12</sup> neutron scattering,<sup>13</sup> group theory,<sup>14</sup> Monte Carlo simulation<sup>15</sup>). Sc-containing layered perovskites have not been widely studied. Indeed, some of the Sc-containing layered perovskites have interesting physical properties such as surprisingly large negative thermal expansion coefficients which exist over a wide range of temperatures.<sup>16–18</sup>

Symmetry and crystallographic analyses of phase transition sequences in layered  $TlAlF_4$ -type crystals were better described in ref. 5 where it was pointed out that such structures realize mostly rotary distortions or pivot-type distortions caused by the rotation of octahedral groups  $BX_6$ . The order parameters (OP) corresponding to librational vibrations of

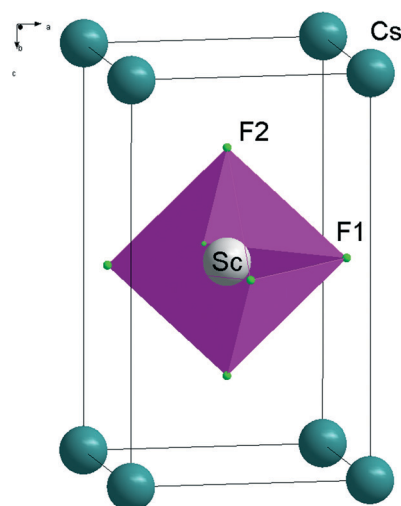


Fig. 1 Crystal structure of CsScF<sub>4</sub> in the  $P4/mmm$  phase.

<sup>a</sup> L. V. Kirensky Institute of Physics, SB RAS, 660036, Krasnoyarsk, Russia.  
E-mail: shusy@iph.krasn.ru

<sup>b</sup> Department of Physics, Far Eastern State Transport University, 680021, Khabarovsk, Russia

<sup>c</sup> Institute of Engineering Physics and Radioelectronics, Siberian Federal University, 660041, Krasnoyarsk, Russia

<sup>d</sup> Institute of Automation and Electrometry, SB RAS, 630090, Novosibirsk, Russia

† Electronic supplementary information (ESI) available. See DOI: 10.1039/c6ce01144f



the octahedra are transformed according irreducible representations (IR) of  $M$  ( $k_{18}$ ) and  $X$  ( $k_{15}$ ) boundary points of the Brillouin zone of the  $D_{4h}^{13}P4/mmm$  group (denotations according to ref. 19 and 20). Distortions associated with condensation of librational modes of  $M$  and  $X$  points are denoted in ref. 5 as distortions of  $\phi$  and  $\psi$  types. Irreducible representations and order parameters inducing symmetry changes are commonly referred to as critical or primary (Fig. 1).

However, in some cases, distortion of the initial phase structure cannot be described by the critical order parameters only. In the distorted (disymmetric) phase, shifts or ordering of atoms should be consistent with the symmetry of this phase and determined by non-critical (secondary) order parameters and irreducible representations. The entire totality of order parameters – critical and noncritical – occurring during phase transition forms a complete order parameter condensate.<sup>21</sup> Group theory analysis<sup>5</sup> of the complete order parameter condensate in crystals with a  $P4/mmm$  parent phase showed that critical distortions of  $\phi$  and  $\psi$  types could be accompanied by noncritical distortions of octahedral groups and noncritical shifts of atoms located between the layers of octahedral groups. Such shifts and distortions are of a secondary nature and could be rather small in the proximity of the phase transition points.

The phase transition sequence in a  $\text{CsScF}_4$  crystal was studied by optical, calorimetric, X-ray and Raman scattering methods.<sup>6,22</sup> It was found<sup>6</sup> to undergo two phase transitions under decreasing temperature; the respective temperatures and basic thermodynamic characteristics are given in Table 1. The experimental data<sup>6,22</sup> gave grounds to make the following conclusions: 1) both phase transitions in  $\text{CsScF}_4$  are of displacement type, 2) the phase transition from  $G_0$  to  $G_1$  is of the first order and that from  $G_1$  to  $G_2$  is of the second order, and 3) distortions are of the form  $(00\psi_z)$  at phase transition  $G_0 \rightarrow G_1$  and  $(\phi_1\phi_2\psi_z)$  at phase transition  $G_1 \rightarrow G_2$ .

However, these conclusions about the form of distortions at the phase transitions were based on indirect data. Besides, the temperature dependence of superstructure reflections oc-

curing in the monoclinic phase which could not be explained by the rotations of octahedral groups only is conspicuous.<sup>6</sup>

To answer the arising questions, experimental Raman scattering, nuclear magnetic resonance and X-ray diffraction studies of the  $\text{CsScF}_4$  crystal have been carried out over a broad temperature range including phase transition temperatures. To interpret the results of the studies, the phase transition sequence was described within the thermodynamic approach.

## 2 Experimental

A clear and transparent  $\text{CsScF}_4$  crystal was grown by using the Bridgman method in a platinum ampoule. The grown crystal had an ideal basal plane of  $(001)_0$ .

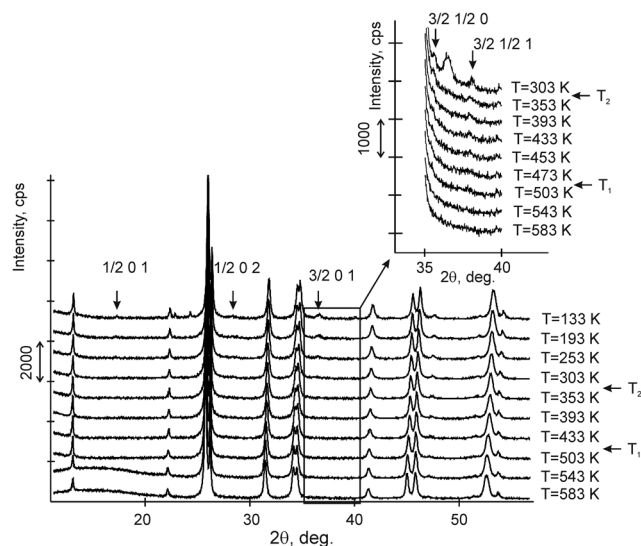
At room temperature,  $\text{CsScF}_4$  single crystals have multiple twins, and therefore, the powder X-ray diffraction (XRD) data were obtained using a Bruker D8 ADVANCE Bragg–Brentano diffractometer with  $\text{Cu-K}\alpha$  radiation. The beam was controlled by a 0.6 mm fixed divergence slit, a 6 mm receiving VANTEC slit and Soller slits. Low- and high-temperature measurements were carried out using an Anton Paar TTK450 attachment.

The variable counting time (VCT) and step size (VSS) schemes were used to collect the diffraction data.<sup>23–26</sup> The total experimental time was 5 hours. There were 10 such experiments performed at different temperatures from 133 to 583 K (Fig. 2).

X-ray analysis of the  $\text{CsScF}_4$  structure at room temperature showed that the grown crystals were free from any impurities.

**Table 1** Principal thermal-physical and crystallographic characteristics of the three phases of  $\text{CsScF}_4$

	$G_2$	$G_1$	$G_0$
PT temperature, K	317.5	475	
Change in the entropy $\Delta S/R$ at PT	0.21	0.16	
Change in the entropy $\delta S/R$ at PT	0	0.11	
Space group	$D_{2h}^{13}-Pmmm$	$D_{4h}^5-P4/mbm$	$D_{4h}^{13}-P4/mmm$
$Z$	4	2	1
$T_{\text{exp}}$ , K	200	400	500
Cell parameters			
$a_i$	$2a_0$	$a_0 + b_0$	$a_0$
	7.944	5.662	4.025
$b_i$	$2b_0$	$-a_0 + b_0$	$b_0$
	7.956	5.662	4.025
$c_i$	$c_0$	$c_0$	$c_0$
	6.763	6.814	6.822



**Fig. 2** X-ray diffraction patterns in the  $2\theta$  region of  $11\text{--}56^\circ$  of  $\text{CsScF}_4$  from 133 to 583 K. At  $T_2 = 317.5$  K, several superstructure reflections corresponding to the  $X$ -point of the Brillouin zone occur. Inset: Superstructure reflections corresponding to the  $M$ -point of the Brillouin zone emerge upon cooling. The indices of all superstructure peaks were calculated using cell parameters of the parent phase, and therefore, they are rational numbers.



The main structural reflections were found to coincide with the orthorhombic symmetry suggested in ref. 5 and 34.

Raman spectra in a backscattering geometry were recorded in a subtractive dispersion mode using a Horiba Jobin Yvon T64000 triple spectrometer equipped with a liquid nitrogen cooled charge coupled device detection system. A Spectra-Physics Stabilite Ar<sup>+</sup> ion laser 2017 with  $\lambda = 514.5$  nm and 5 mW power on the sample was used as an excitation light source.

Temperature measurements were carried out using a closed cycle ARS CS204-X1.SS helium cryostat in the temperature range of 10–295 K. The temperature was monitored by using a LakeShore DT-6SD1.4L silicon diode. During experiments, the cryostat was evacuated to  $10^{-6}$  mbar. To investigate the low-wavenumber spectra, measurements down to  $6\text{ cm}^{-1}$  were performed in a subtractive dispersion mode. Deformation of the low-wavenumber spectral edge by the optical slit, which sometimes smears the true features of the low-wavenumber spectra, was carefully eliminated by rigorous optical alignment. The CCD pixel coverage in an additive dispersion mode was as fine as  $0.3\text{ cm}^{-1}$ , but it was limited by the spectrometer spectral resolution of  $1.8\text{ cm}^{-1}$ .

The temperature experiments were carried out in a dynamic mode varying the sample temperature at the rate of  $0.5\text{ K min}^{-1}$ . The uncertainty of the measured temperature for a given rate can be estimated as the difference between the adjacent measurements and it was  $\pm 0.12\text{ K}$  in one spectrum measurement. The overall time for a single spectrum accumulation was within 30 s. The spectra were acquired with a temperature step of  $0.25\text{ K}$ . This measurement protocol was the same as described in ref. 27 and 28.

The high temperature (above 320 K) and polarized Raman experiments were carried out using a laser beam focused on the sample by a  $50\times$  Olympus LMPlanFl objective lens with a numerical aperture (NA) of 0.5. The power of the incident laser light was 5 mW on the sample. The scattered light was collected by the same objective lens in a backscattering geometry and analyzed using a polarizer and a  $\lambda$ -plate. The temperature of the samples was controlled by using a Linkam THMS600 microstat with the stability of  $<\pm 0.2\text{ K}$ .

Infrared spectra were obtained in the temperature range from 15 to 300 K using a vacuum Vertex 80 spectrometer. A  $3 \times 3\text{ mm}$  and  $50\text{ }\mu\text{m}$  thick crystal plate was used as a sample.

NMR studies of CsScF<sub>4</sub> crystals were carried out on all magnetic nuclei in the crystal. NMR spectra of <sup>19</sup>F, <sup>45</sup>Sc and <sup>133</sup>Cs nuclei were recorded using an AVANCE 300 pulse NMR spectrometer by Fourier spectroscopy (Larmor frequencies for <sup>19</sup>F nuclei – 282.4 MHz, for <sup>45</sup>Sc nuclei – 72.9 MHz, and for <sup>133</sup>Cs nuclei – 39.4 MHz, the 90° pulse time was 2.9  $\mu\text{s}$  for fluorine and about 1  $\mu\text{s}$  for scandium and cesium).

The Brillouin scattering spectra were measured in a backscattering geometry using 3 + 3 pass Sandercock tandem Fabry–Perot interferometers.<sup>29</sup> The distance between the interferometer mirrors was 5 mm corresponding to the free dispersion range of 30 GHz. The radiation source was a solid state 200 mW, 532 nm laser. The reference beam was isolated

after reflection of the primary laser radiation from a thin glass plane and was used to adjust the spectrometer and stabilize its operation during measurements. After passing the glass plane, the characteristic laser radiation was directed by a prism (PR) (2 mm) onto the sample under study. An achromatic lens (L<sub>1</sub>) with a focal length of 150 mm both focused the radiation onto the sample and collected the scattered signal. The scattered radiation was focused on the input diaphragm of the spectrometer by a lens (L<sub>2</sub>) with a focal length of 400 mm. The sizes of the input and output diaphragms were 450 and 700  $\mu\text{m}$ , respectively. The periscope mirrors M<sub>1</sub> and M<sub>2</sub> were used for vertical and horizontal adjustments to put the scattered radiation into the spectrometer.

### 3 Determination of crystal structures

Earlier<sup>5</sup> it was supposed that the crystal has the phase transition

$$\text{sequence } P4/mmm \xrightarrow{M3+(\eta)} P4/mbm \xrightarrow{M3+(\eta) \otimes X3+(\xi_1, \xi_2)} Pmmn.$$

We believe that these designations of irreducible representations (irrep) are incorrect. In reality,  $M3+(k18t3)$  and  $X3+(k15t3)$  irreps lead to distortion of the ScF<sub>6</sub> octahedron (Fig. 3). The analysis shows that only  $M2+(k18t5)$  and  $X2-(k15t8)$  lead to the rotation of the ScF<sub>6</sub> octahedron (Fig. 3), so  $M2+$  and

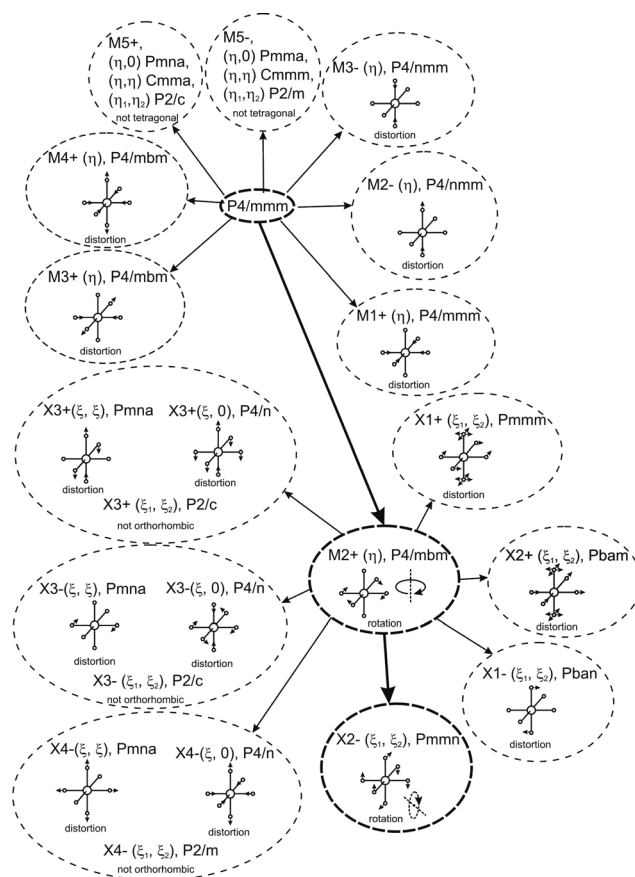


Fig. 3 Group-subgroup graph with possible distortion of the ScF<sub>6</sub> octahedron. Phase transitions allowing the rotation of the ScF<sub>6</sub> octahedron are shown by a bold line.



**Table 2** Main bond lengths of CsScF<sub>4</sub>

Bond length	
<i>T</i> = 133 K, <i>Pmmn</i>	
Sc–F3	1.934(5)
Sc–F1	2.018(4)
Sc–F2	2.049(5)
Cs1–F3	3.07(1)
Cs1–F2	3.27(2)
Cs1–F3	3.30(1)
Cs2–F3	3.07(1)
Cs2–F3	3.29(1)
<i>T</i> = 193 K, <i>Pmmn</i>	
Sc–F3	1.935(4)
Sc–F1	2.026(4)
Sc–F2	2.034(4)
Cs1–F3	3.08(1)
Cs1–F2	3.29(1)
Cs1–F3	3.36(2)
Cs2–F3	3.06(1)
Cs2–F3	3.30(1)
<i>T</i> = 253 K, <i>Pmmn</i>	
Sc–F3	1.934(5)
Sc–F1	2.024(5)
Sc–F2	2.033(5)
Cs1–F3	3.10(2)
Cs1–F2	3.28(2)
Cs1–F3	3.41(3)
Cs2–F3	3.07(2)
Cs2–F3	3.30(2)
<i>T</i> = 303 K, <i>Pmbm</i>	
Sc–F3	1.926(4)
Sc–F1	2.017(4)
Sc–F2	2.022(5)
Cs1–F3	3.16(2)
Cs1–F2	3.22(2)
Cs1–F3	3.57(3)
Cs2–F3	3.15(2)
Cs2–F3	3.23(2)
<i>T</i> = 353 K, <i>P4/mbm</i>	
Sc–F2	1.914(4)
Sc–F1	2.023(6)
Cs–F2	3.196(2)
<i>T</i> = 393 K, <i>P4/mbm</i>	
Sc–F2	1.911(5)
Sc–F1	2.020(6)
Cs–F2	3.201(2)
<i>T</i> = 433 K, <i>P4/mbm</i>	
Sc–F2	1.902(2)
Sc–F1	2.020(6)
Cs–F2	3.209(2)
<i>T</i> = 503 K, <i>P4/mmm</i>	
Sc–F2	1.923(5)
Sc–F1	2.009(1)
Cs–F2	3.207(3)
<i>T</i> = 543 K, <i>P4/mmm</i>	
Sc–F2	1.913(5)
Sc–F1	2.013(1)
Cs–F2	3.217(2)

**Table 2 (continued)**

Bond length	
<i>T</i> = 583 K, <i>P4/mmm</i>	
Sc–F2	1.913(5)
Sc–F1	2.016(1)
Cs–F2	3.222(2)

X2<sup>−</sup> should be critical irreps instead. In addition, such a sequence of irreps agrees with the sequence of space groups,

$P4/mmm \xrightarrow{M2+ (\eta)} P4/mbm \xrightarrow{M2+ (\eta) \otimes X2- (\xi_1, \xi_2)} Pmmn$ , found earlier.<sup>5</sup>

Comparison of powder diffraction data shows that the structure has changed at 460–475 K where superstructure peaks emerge corresponding to the *M*-point of the Brillouin zone (Fig. 2) and at *T*<sub>2</sub> = 317.5 K where several superstructure peaks of the *X*-point of the Brillouin zone emerge. This confirms that the phase transition at *T*<sub>1</sub> = 475 K is associated with the appearance of the order parameter (OP) of the *M* irreducible representation and the next phase transition at *T*<sub>2</sub> = 317.5 K is associated with the OP of the *X* irreducible representation. As ScF<sub>6</sub> can be rotated by *M*2<sup>+</sup> and *X*2<sup>−</sup> only, it was decided to refine the crystal structure considering *M*2<sup>+</sup> and *X*2<sup>−</sup> as critical irreducible representations.

The crystal structure of the low temperature phases was solved by distortion-mode refinement of the X-ray data using TOPAS 4.2 program, with the file generated by ISO-DISPLACE.<sup>30,31</sup> Space groups *P4/mbm* and *Pmmn* were used. There are two OPs associated with all displacements of atoms, *GM*1<sup>+</sup> (*a*) and *M*2<sup>+</sup> (*η*), for the *P4/mbm* phase and nine OPs, *GM*1<sup>+</sup> (*a*), *M*1<sup>+</sup> (*b*), *M*2<sup>+</sup> (*η*), and six OPs, *X*2<sup>−</sup> (*ξ*<sub>1</sub>, *ξ*<sub>2</sub>), for the *Pmmn* phase. *M*2<sup>+</sup> acts on 2e sites occupied by F and leads to the rotation of the ScF<sub>6</sub>, while *X*2<sup>−</sup> acts on F sites and Cs sites. *M*1<sup>+</sup> leads to distortion of the ScF<sub>6</sub> octahedron. All the respective amplitudes were used to find a model structure by using the simulated annealing method. The refinement yielded satisfactory final *R*-factors (Table 3), interatomic distances as well as thermal parameters. The Rietveld difference plot of CsScF<sub>4</sub> at 303 K is shown in Fig. 4. All other results within the range of 133–583 K are given in the ESI.† The thermal parameter of the Cs ion was refined in an anisotropic model. The atomic coordinates and isotropic thermal parameters can be found in Table 4 and the main bond lengths in Table 2. One can see that the thermal parameters increase evenly upon heating. This is indicative of the absence of any order–disorder process at phase transitions and proves the suggestion<sup>5</sup> that the mechanisms of phase transitions have a displacive distortion nature. The difference between the lengths of Sc–F bonds is small (maximum 0.115 Å) and the F–Sc–F angles in the octahedron range within 87–93°. Thus, the ScF<sub>6</sub> octahedron does not undergo strong distortions at phase transitions. This agrees with the earlier conclusions.<sup>5,22,32–34</sup>





**Table 3** Main refinement parameters

<i>T</i> , K	Sp. gr.	<i>a</i> <sub>i</sub> , Å	<i>b</i> <sub>i</sub> , Å	<i>c</i> <sub>i</sub> , Å	<i>V</i> , Å <sup>3</sup>	<i>Z</i>	<i>R</i> <sub>wp</sub> , %	<i>R</i> <sub>B</sub> , %
133	<i>Pmmn</i>	7.9561(5)	7.9545(5)	6.7557(3)	427.55(5)	4	6.26	1.89
193	<i>Pmmn</i>	7.9663(5)	7.9630(4)	6.7668(3)	429.25(4)	4	5.35	1.50
253	<i>Pmmn</i>	7.9783(5)	7.9748(5)	6.7814(3)	431.46(4)	4	5.84	1.52
303	<i>Pmmn</i>	7.9878(5)	7.9832(4)	6.7936(2)	433.21(4)	4	4.43	1.41
353	<i>P4/mbm</i>	5.6538(2)		6.8076(3)	217.60(1)	2	5.97	1.55
393	<i>P4/mbm</i>	5.6601(2)		6.8135(3)	218.28(2)	2	5.50	1.37
433	<i>P4/mbm</i>	5.6667(2)		6.8180(3)	218.94(2)	2	6.21	1.62
503	<i>P4/mmm</i>	4.0175(1)		6.8226(3)	110.117(9)	1	5.91	1.82
543	<i>P4/mmm</i>	4.0260(1)		6.8233(3)	110.599(9)	1	4.94	1.91
583	<i>P4/mmm</i>	4.0317(2)		6.8282(4)	110.99(1)	1	5.15	2.03

Complete mode details of distorted structures show the following temperature dependences of displacive mode amplitudes (Fig. 5). It is obvious that OP ( $\eta$ ) of  $M2+$  irrep is critical as it has maximal values. It emerges jumpwise at  $T_1 = 475$  K which accounts for a first order transition and increases upon further cooling. New critical OPs ( $\eta_1$ ,  $\xi_2$ ) appear at  $T_2 = 317.5$  K and increase rapidly upon cooling.  $GM1+$  ( $a$ ) and  $M1+$  ( $b$ ) are noncritical.

The primitive cell volume is doubled at the first phase transition  $P4/mmm \xrightarrow{M2+(\eta)} P4/mbm$  (Fig. 6). The cell parameters are transformed:  $a_1 = a_0 + b_0$ ;  $b_1 = b_0 - a_0$ ;  $c_1 = c_0$  ( $a_1$ ,  $b_1$ , and  $c_1$  are the basis vectors of the distorted  $P4/mbm$  phase, and  $a_0$ ,  $b_0$ , and  $c_0$  are the basis vectors of the parent  $P4/mbm$  phase), and the origin shift is  $(1/2, 1/2, 0)$ . The  $ScF_6$  octahedra with a common node are rotated on  $\phi \sim \eta$  in opposite directions. There are no other rotations or heavy atom displacement.

At the second phase transition  $P4/mbm \xrightarrow{M2+(\eta) \otimes X2-(\xi_1, \xi_2)} Pmmn$ , the primitive cell volume increases 4 times. Position 1a occupied by Cs is split into two: Cs1 and Cs2. The cell parameters are transformed as follows:  $a_2 = 2a_0$ ;  $b_2 = 2b_0$ ;  $c_2 = c_0$  ( $a_2$ ,  $b_2$ , and  $c_2$  are the basis vectors of the distorted  $Pmmn$  phase, and  $a_0$ ,  $b_0$ , and  $c_0$  are the basis vectors of the parent  $P4/mbm$  phase). The rotation on  $\phi \sim \eta$  goes on, and two new rotations appear: around the  $\bar{a} + \bar{b}$  axis on angle  $\psi_1 \sim \xi_1$  and around the  $\bar{a} - \bar{b}$  axis on angle  $\psi_2 \sim \xi_2$  (Fig. 6). The new OPs ( $\xi_1$ ,  $\xi_2$ ) make the Cs1 and Cs2 atoms move along the  $c$  axis.

A detailed analysis of the OP and irreps in the program ISOTROPY<sup>30</sup> shows that  $M2+(\eta)$  and  $X2-(\xi_1, \xi_2)$  induce the phase transition that could be a second order phase transition. In fact, the phase transition at  $T_1 = 475$  K is of a first order type, and at  $T_2 = 317.5$  K, it is of a second order type.<sup>5,22,32–34</sup>

## 4 Vibrational spectroscopy

### 4.1 The selection rules

To describe the results of the Raman and infrared experiments, we performed a symmetry analysis of the vibrational modes in all phases. The selection rules, classification of

modes, Wyckoff positions, irreducible representations and Raman tensors for all three phases are presented in Table 5. The fractional atomic coordinates are taken from Table 4. The Raman mode representation for the tetragonal phase  $P4/mbm$  at temperatures above 475 K at the Brillouin zone center is

$$\Gamma_{\text{Raman}} = A_{1g} + E_g \quad (1)$$

The infrared mode representation is

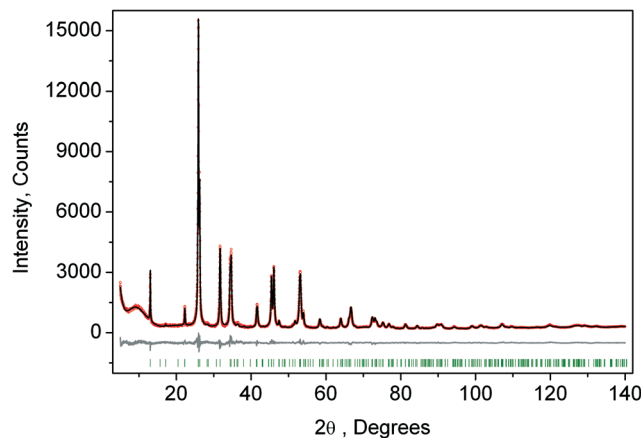
$$\Gamma_{\text{IR}} = 3A_{2u} + 4E_u \quad (2)$$

It is reasonable to expect two modes in the Raman spectra, seven active modes in the infrared spectra, and acoustic modes. The Raman mode representation for the tetragonal phase  $P4/mbm$  at temperatures above 317.5 K and below 475 K at the Brillouin zone center is

$$\Gamma_{\text{Raman}} = 2A_{1g} + B_{1g} + B_{2g} + 3E_g \quad (3)$$

The infrared mode representation is

$$\Gamma_{\text{IR}} = 3A_{2u} + 7E_u \quad (4)$$



**Fig. 4** Rietveld difference plot of  $CsScF_4$  at 303 K ( $Pmmn$  phase). The other plot is presented in the ESI.†



**Table 4** Fractional atomic coordinates and isotropic (\* – equivalent) displacement parameters ( $\text{\AA}^2$ ) of  $\text{CsScF}_4$ 

	<i>x</i>	<i>y</i>	<i>z</i>	Biso, $\text{\AA}^2$
<i>T</i> = 133 K, <i>Pmmn</i>				
Cs1	1/4	1/4	−0.0285(5)	2.5(1)* $U_{11} = 0.054(4)$ , $U_{22} = 0.020(4)$ , $U_{33} = 0.020(3)$
Cs2	1/4	3/4	−0.001(2)	2.6(1)* $U_{11} = 0.023(4)$ , $U_{22} = 0.020(4)$ , $U_{33} = 0.055(4)$
Sc	0	0	1/2	1.4(1)
F1	1/4	0.540(3)	0.515(3)	1.9(2)
F2	0.044(3)	1/4	0.552(3)	1.9(2)
F3	0.491(2)	0.469(2)	0.2164(6)	1.9(2)
<i>T</i> = 193 K, <i>Pmmn</i>				
Cs1	1/4	1/4	−0.0259(5)	3.0(1)* $U_{11} = 0.069(3)$ , $U_{22} = 0.020(4)$ , $U_{33} = 0.025(3)$
Cs2	1/4	3/4	−0.004(2)	3.0(1)* $U_{11} = 0.027(3)$ , $U_{22} = 0.020(4)$ , $U_{33} = 0.067(3)$
Sc	0	0	1/2	1.7(1)
F1	1/4	0.546(3)	0.515(3)	2.4(2)
F2	0.032(3)	1/4	0.549(3)	2.4(2)
F3	0.493(2)	0.471(2)	0.2162(6)	2.4(2)
<i>T</i> = 253 K, <i>Pmmn</i>				
Cs1	1/4	1/4	−0.0224(8)	3.5(2)* $U_{11} = 0.074(5)$ , $U_{22} = 0.020(5)$ , $U_{33} = 0.037(4)$
Cs2	1/4	3/4	−0.005(2)	3.6(1)* $U_{11} = 0.049(5)$ , $U_{22} = 0.020(5)$ , $U_{33} = 0.066(5)$
Sc	0	0	1/2	1.7(2)
F1	1/4	0.542(4)	0.509(4)	2.7(2)
F2	0.033(4)	1/4	0.544(4)	2.7(2)
F3	0.494(2)	0.474(2)	0.2166(6)	2.7(2)
<i>T</i> = 303 K, <i>Pmmn</i>				
Cs1	1/4	1/4	−0.0191(6)	4.3(2)* $U_{11} = 0.094(5)$ , $U_{22} = 0.020(4)$ , $U_{33} = 0.047(5)$
Cs2	1/4	3/4	0.002(2)	3.55(1)* $U_{11} = 0.061(5)$ , $U_{22} = 0.020(4)$ , $U_{33} = 0.068(5)$
Sc	0	0	1/2	3.9(2)
F1	1/4	0.539(4)	0.508(4)	3.8(2)
F2	0.031(4)	1/4	0.523(4)	3.8(2)
F3	0.495(2)	0.486(2)	0.2170(5)	3.8(2)
<i>T</i> = 353 K, <i>P4/mbm</i>				
Cs	0	1/2	0	3.97(8)* $U_{11} = U_{22} = 0.036(2)$ , $U_{33} = 0.078(2)$ , $U_{12} = 0.015(2)$
Sc	0	0	1/2	1.9(1)
F1	0.711(1)	0.211(1)	1/2	4.2(2)
F2	0	0	0.2189(7)	4.2(2)
<i>T</i> = 393 K, <i>P4/mbm</i>				
Cs	0	1/2	0	4.2(1)* $U_{11} = U_{22} = 0.038(2)$ , $U_{33} = 0.084(2)$ , $U_{12} = -0.015(2)$
Sc	0	0	1/2	1.9(1)
F1	0.716(1)	0.216(1)	1/2	4.2(2)
F2	0	0	0.2195(7)	4.2(2)
<i>T</i> = 433 K, <i>P4/mbm</i>				
Cs	0	1/2	0	4.7(1)* $U_{11} = U_{22} = 0.043(2)$ , $U_{33} = 0.091(2)$ , $U_{12} = 0.001(3)$
Sc	0	0	1/2	2.0(2)
F1	0.718(1)	0.218(1)	1/2	4.3(2)
F2	0	0	0.2211(8)	4.3(2)
<i>T</i> = 503 K, <i>P4/mmm</i>				
Cs	0	0	0	4.7(1)* $U_{11} = U_{22} = 0.042(2)$ , $U_{33} = 0.094(2)$ , $U_{12} = 0.011(1)$
Sc	1/2	1/2	1/2	2.0(2)
F1	0	1/2	1/2	5.4(2)
F2	1/2	1/2	0.2182(8)	5.4(2)
<i>T</i> = 543 K, <i>P4/mmm</i>				
Cs	0	0	0	5.1(1)* $U_{11} = U_{22} = 0.046(2)$ , $U_{33} = 0.101(2)$ , $U_{12} = 0.013(1)$
Sc	1/2	1/2	1/2	2.0(2)
F1	0	1/2	1/2	5.4(2)
F2	1/2	1/2	0.2196(7)	5.4(2)
<i>T</i> = 583 K, <i>P4/mmm</i>				
Cs	0	0	0	5.8(1)* $U_{11} = U_{22} = 0.055(2)$ , $U_{33} = 0.112(2)$ , $U_{12} = 0.014(2)$
Sc	1/2	1/2	1/2	2.9(1)
F1	0 1/2	1/2	6.2(2)	
F2	1/2	1/2	0.2199(7)	6.2(2)



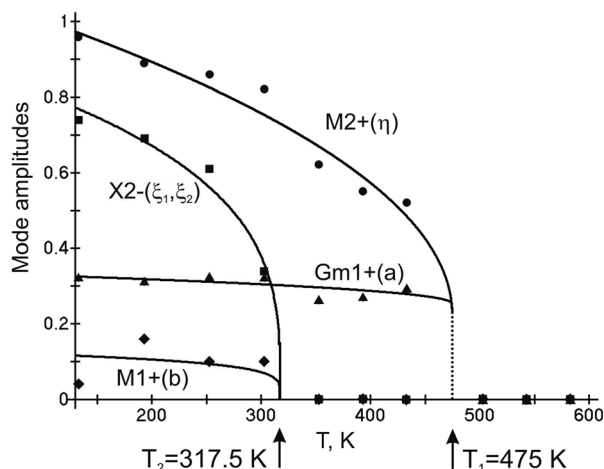


Fig. 5 Displacive mode amplitudes.

It is reasonable to expect 7 modes in the Raman spectra, 10 active modes in the infrared spectra, and acoustic modes. The Raman mode representation for the orthorhombic phase *Pmmn* at temperatures below 317.5 K at the Brillouin zone center is

$$\Gamma_{\text{Raman}} = 9A_g + 5B_{1g} + 8B_{2g} + 8B_{3g} \quad (5)$$

The infrared mode representation is

$$\Gamma_{\text{IR}} = 11B_{1u} + 10B_{2u} + 10B_{3u} \quad (6)$$

It is reasonable to expect 30 modes in the Raman spectra, 31 active modes in the infrared spectra, and 3 acoustic modes.

## 4.2 Raman and IR

To analyze the low wavenumber Raman spectra quantitatively, we performed a spectral analysis with a combination of conventional damped harmonic oscillator functions:<sup>35,36</sup>

$$I(\omega) = F(\omega, T) \sum_i \frac{2A_i \omega_i^2 \gamma_i \omega}{(\omega_i^2 - \omega^2)^2 + 4\gamma_i^2 \omega^2} \quad (7)$$

where  $\omega_0$  is the current wavenumber,  $A$ ,  $\omega$  and  $\Gamma$  denote the intensity, harmonic wavenumber of the band centre and full width at half maximum, respectively, of the corresponding excitation indicated by the subscript. The temperature factor  $F(\omega, T)$  is calculated by

$$F(\omega, T) = \begin{cases} n(\omega) + 1 & \text{Stokes} \\ n(\omega) & \text{Anti-Stokes} \end{cases} \quad (8)$$

$$n(\omega) = \left[ \exp\left(\frac{\hbar\omega}{k_B T}\right) - 1 \right]^{-1} \quad (9)$$

where  $\hbar$ ,  $k_B$  in eqn (9) denote the reduced Planck constant,

the Boltzmann constant, respectively. The present Raman setup can see only the Stokes component.

The high symmetry phase studied earlier using Raman spectra<sup>32</sup> exhibits two vibrations in the spectrum: at  $495 \text{ cm}^{-1}$  ( $A_{1g}$ ) and  $152 \text{ cm}^{-1}$  ( $E_g$ ) just as was predicted by the selection rules (Table 5). The experimental Raman data, numerical simulation and normal vibrational mode representations for the *P4/mbm* phase are given in Table 8. These vibrations are the vibrations of axial fluorine atoms. After the first phase transition, vibrations emerge mostly because of the restructuring of the Brillouin zone; as a result, part of the vibrations from the *M* point become Raman-active. We observe seven vibrations:  $32 \text{ cm}^{-1}$  ( $E_g$ ),  $107 \text{ cm}^{-1}$  ( $A_{1g}$ ),  $152 \text{ cm}^{-1}$  ( $E_g$ ),  $188 \text{ cm}^{-1}$  ( $B_{1g}$ ),  $233 \text{ cm}^{-1}$  ( $E_g$ ),  $255 \text{ cm}^{-1}$  ( $B_{2g}$ ),  $495 \text{ cm}^{-1}$  ( $A_{1g}$ ). These vibrations are not associated with vibrations of heavy ions but for vibrations of fluorine ions only (Table 5). The experimental Raman data, numerical simulation and normal vibrational mode representations for the *P4/mbm* phase can be found in Table 9.

An overview of the experimental spectra of all components of the Raman tensor in all phases is shown in Fig. 7. The temperatures of the spectra in the figure were chosen rather far from the phase transition points. The spectra of the intermediate phase *P4/mbm* at 393 K are in fairly good agreement with the ones previously published.<sup>32</sup>

The condensation of soft modes after both phase transitions is the most significant observed result, which is presented in Fig. 8. The plot showing the dependence of wavenumber vs. temperature is shown in Fig. 9. The Raman spectra include several modes demonstrating soft mode

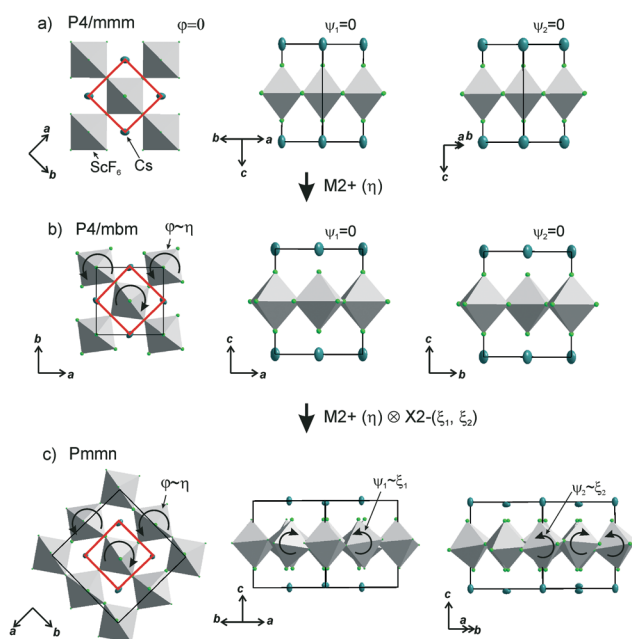


Fig. 6 Different projections of the crystal structure: (a) tetragonal *P4/mbm* parent phase,  $\text{ScF}_6$  doesn't rotate; (b) tetragonal *P4/mbm* distorted phase,  $\text{ScF}_6$  rotates on  $\phi$  around the *c*-axis; (c) orthorhombic *Pmmn* distorted phase,  $\text{ScF}_6$  rotates on  $\phi$  around the *c*-axis and rotates on  $\psi_1$ ,  $\psi_2$  around the *a* + *b* axis and the *a* − *b* axis, respectively.



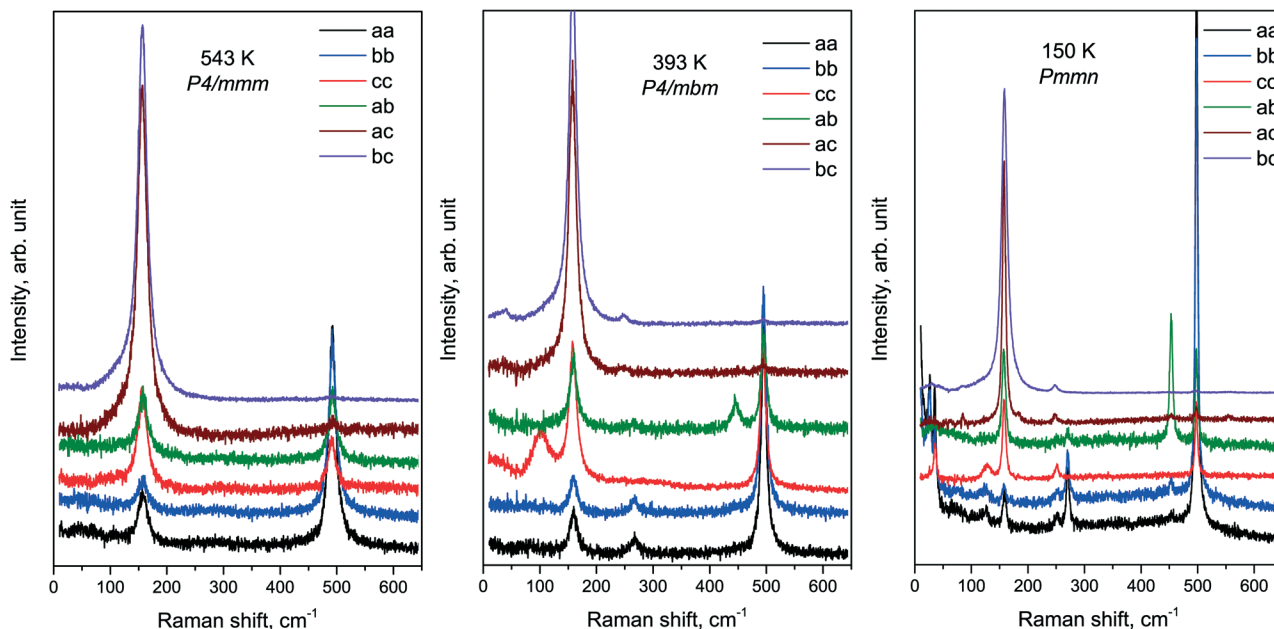


Fig. 7 Polarized Raman spectra: of all three phases.

behavior: one ( $E_g$  33  $\text{cm}^{-1}$  at 393 K) below the first phase transition at  $T_1 = 478$  K and two ( $A_g$  37  $\text{cm}^{-1}$  and 56  $\text{cm}^{-1}$  at 193 K) below the second phase transition at  $T_1 = 317.5$  K. These data are in good agreement with the conclusion based on the XRD experiments. The results of empirical vibrational

spectra simulation show that these soft modes correspond to rotations of the  $\text{ScF}_6$  octahedral group (see Table 10).

The transformation of the IR spectra at temperatures below 700  $\text{cm}^{-1}$  is shown in Fig. 10. Table 6 compares the experimental and calculated data for a crystal in the  $Pmmn$  phase.

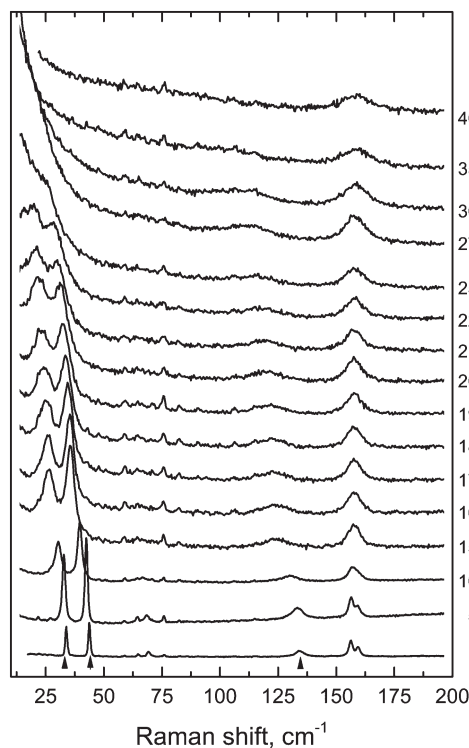


Fig. 8 Temperature evolution of the Raman spectra of  $\text{CsScF}_4$ . The arrow indicates the soft modes.

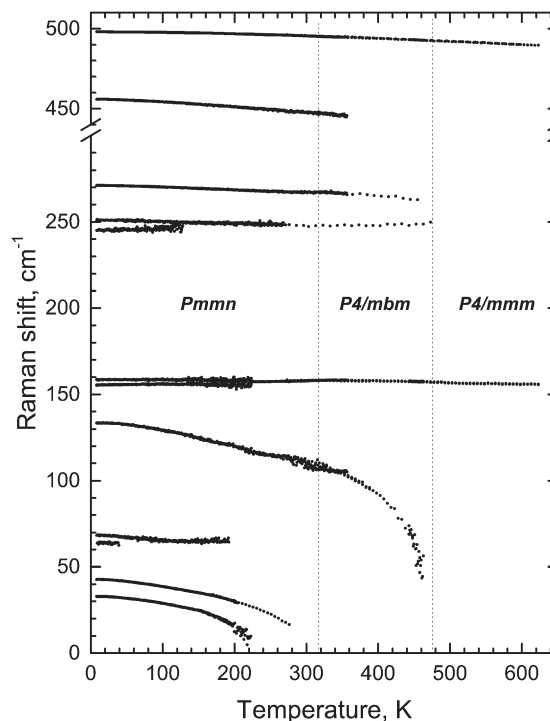


Fig. 9 Temperature dependence of the most intense Raman lines.





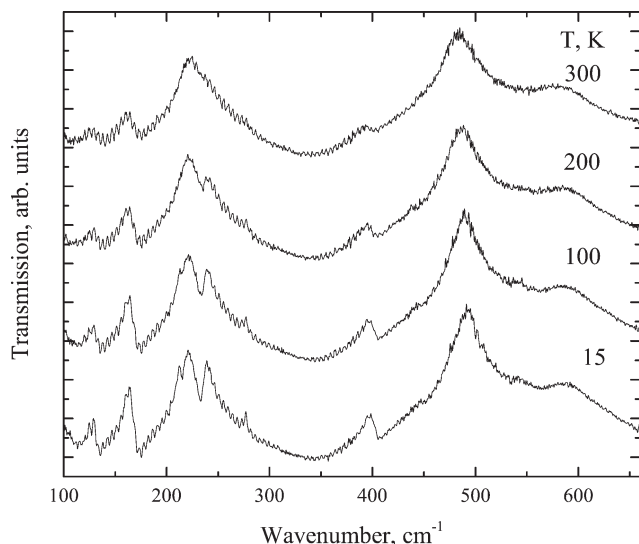


Fig. 10 IR spectra transformation with increasing temperature in the *Pmmn* phase.

#### 4.3 Vibrational spectra simulation

The lattice dynamics of  $\text{CsScF}_4$  in all phases was simulated in terms of the Born-Karman model using LADY software.<sup>37,38</sup> Within this model, only pair-wise interactions and bond-stretching force constants are considered. A simplified version of the Born-Karman model implies that the bond-stretching force constant  $A$  depend on  $R$  only ( $R$  is the bond length), and the  $A(R)$  dependences are the same for all atom pairs:

$$A = \lambda e^{\left(\frac{-R_0}{\rho}\right)}, \quad (10)$$

where  $\lambda$  and  $\rho$  are the parameters describing the interaction of selected pairs. To find the parameters of the model, a special optimization software was written and tested for several compounds.<sup>39–45</sup> The initial values of the parameters were set within the ranges typical for perovskite-like fluorides. The lattice stability conditions were taken into account. The final model parameters were obtained by minimization of residual values of the simulated and experimental Raman wavenumbers by using the Fletcher-Reeves method. In the case of optimization pending due to incompatibility of the model parameters, the initial parameters of the model were changed randomly. The parameters obtained for the Born-Karman model at 543 K are given in Table 7. The structural data of all phases were taken from Tables 3 and 4. Comparison of the simulated and experimental wavenumbers of the Raman lines is presented in Table 8.

#### 4.4 Brillouin light scattering

Fig. 11 shows a typical Brillouin scattering spectrum measured in the crystal under study at a temperature of 296 K. To define positions and linewidths, each of the Brillouin

components is described by a Voigt function with a free Gauss parameter. A fitting example is given in Fig. 11 in red.

Fig. 12 shows the experimentally obtained temperature dependences of the position and width (FWHM) of the Brillouin components. At  $\sim 311$  K, the temperature dependences of both parameters exhibit a distinctive feature indicating a phase transition. Such a behavior is typical for second order structural phase transitions. Another feature is observed as a kink at about 480 K. The magnitude of the effect is relatively small, but it allows us to confidently claim the existence of the first order phase transition. The lack of drastic changes in the elastic parameters of the material may be an indication of the lack of changes in the structure of the crystal lattice at this temperature. Such features take place in glass when additional degrees of freedom of molecules are defrosted during heating of the sample.

## 5 NMR

Temperature dependences of the  $^{19}\text{F}$  NMR spectra were experimentally studied with a single crystal sample in the temperature range of 290–585 K. With the external magnetic field oriented along the  $c$ -axis of the crystal, the NMR spectrum of  $^{19}\text{F}$  at room temperature consists of two lines of equal intensities. When the crystal is rotated around the  $a$  axis, one of these lines splits into two; the splitting is maximal when the magnetic field is normal to the  $c$  axis. This behavior leads to the conclusion that these lines belong to two magnetically nonequivalent fluorine atoms in the equatorial plane of the  $\text{ScF}_6$  octahedron. It is impossible to obtain parameter values of the chemical shielding tensors from orientation dependences of poorly resolvable NMR spectra of  $^{19}\text{F}$ ; we can only suppose that they correspond to the polar and equatorial fluorine atoms. The obtained NMR spectra of  $^{19}\text{F}$  vary very little in the temperature range from 290 to 510 K, including both phase transitions. Taking into consideration the results of X-ray structural studies, such a result is quite expected, because the bond lengths of the  $\text{ScF}_6$  octahedron practically do not change in transitions, and accordingly, the parameters of magnetic shielding of fluorine atoms change insignificantly. As for the parameters of the dipole-dipole interaction (manifested, first of all, in the width of individual lines), their invariability is indicative of the lack of mobility of fluorine ions in the structure. However, the NMR  $^{19}\text{F}$  lines were found to broaden with further heating (above 510 K), and above 530 K, all the lines merge into a single line in the centroid of the  $^{19}\text{F}$  NMR spectrum; its width decreases with increasing temperature (Fig. 13). Such changes in the spectrum are typical of an exchange process, in this case the exchange between polar and equatorial fluorine atoms. The emergence of a single line corresponds to the frequency of exchange approximately equal to the line splitting value in the  $^{19}\text{F}$  NMR spectrum.

Thus, the temperature dependence in Fig. 13 allows the exchange rate  $\nu \sim 10^4$  Hz to be evaluated at  $T = 530$  K. Further narrowing of the lines with increasing temperature is



associated with diffusion of fluorine atoms over the crystal lattice sites.

The spin of  $^{45}\text{Sc}$  and  $^{133}\text{Cs}$  nuclei is  $I = 7/2$ , and unlike the  $^{19}\text{F}$  nuclei, they have electric quadrupole moments. NMR makes it possible to obtain information about the value and symmetry of gradients of crystalline electric fields at the site of the nucleus under study. In the low-temperature phase, there is one structurally nonequivalent scandium atom (position 4d) in a unit cell. However, in general orientation, each of the seven components of the NMR spectrum of  $^{45}\text{Sc}$  splits into four lines. Consequently, in a unit cell of  $\text{CsScF}_4$ , there are four magnetically nonequivalent positions of scandium ions. The analysis of orientation dependences of the NMR spectrum of  $^{45}\text{Sc}$  made it possible to find the three-axial tensor of the electric-field gradient (EFG) at the site of the scan-

dium ion with the main value  $V_{zz} = 3.41$  MHz and asymmetry parameter  $\eta \approx 0.1$ . The principal axis  $V_{zz}$  of the EFG tensor is tilted from the  $c$  axis of the crystal by about  $10^\circ$  at room temperature (292 K). Under heating, the tilt angle gradually decreases, so does the asymmetry parameter, and at phase transition temperature  $T_2 = 317$  K, the EFG tensor becomes axially-symmetrical in compliance with the point symmetry of the scandium ion position (2b) in the intermediate phase. Fig. 14 shows temperature evolution of  $^{45}\text{Sc}$  NMR spectrum lines belonging to transition  $3/2 \leftrightarrow 1/2$ . Over the entire temperature range of existence of the intermediate phase, the principal value of  $V_{zz} = 3.41$  MHz of the axially symmetrical EFG tensor does not change (Fig. 14). This value does not change in the transition to the high-temperature phase ( $T_1 = 475$  K), either. Even though in this phase transition the point

**Table 5** Wyckoff positions, irreducible representations, and Raman tensors ( $\Gamma$ -point phonon modes) for  $\text{CsScF}_4$  (space groups  $P4/mmm$ ,  $P4/mbm$ ,  $Pmmn$ )

Atom	Wyckoff position	$\Gamma$ -point phonon modes
<b><math>P4/mmm</math> (123) <math>D_{4h}^1</math></b>		
Cs	1a	$A_{2u} + E_u$
Sc	1d	$A_{2u} + E_u$
F1	2e	$A_{2u} + 2E_u + B_{2u}$
F2	2h	$A_{1g} + E_g + A_{2u} + E_u$
<b>Mode classifications</b>		
$\Gamma_{\text{Raman}} = A_{1g} + E_g$ , $\Gamma_{\text{IR}} = 3A_{2u} + 4E_u$ , $\Gamma_{\text{Acoustic}} = A_{2u} + E_u$ , $\Gamma_{\text{Mech}} = A_{1g} + E_g + 4A_{2u} + 5E_u + B_{2u}$		
<b>Raman tensor</b>		
$A_{1g} = \begin{bmatrix} a & 0 & 0 \\ 0 & a & 0 \\ 0 & 0 & b \end{bmatrix}$ $E_g = \begin{bmatrix} 0 & 0 & 0 \\ 0 & 0 & e \\ 0 & e & 0 \end{bmatrix}$ $E_g = \begin{bmatrix} 0 & 0 & -e \\ 0 & 0 & 0 \\ -e & 0 & 0 \end{bmatrix}$ $B_{1g} = \begin{bmatrix} c & 0 & 0 \\ 0 & -c & 0 \\ 0 & 0 & 0 \end{bmatrix}$ $B_{2g} = \begin{bmatrix} 0 & d & 0 \\ d & 0 & 0 \\ 0 & 0 & 0 \end{bmatrix}$		
<b><math>P4/mbm</math> (127) <math>D_{4h}^5</math></b>		
Cs	2d	$A_{2u} + 2E_u + B_{1u}$
Sc	2b	$A_{2u} + 2E_u + A_{1u}$
F1	4h	$A_{1g} + E_g + A_{2u} + 2E_u + A_{2g} + B_{1g} + B_{1u} + B_{2g}$
F2	4c	$A_{1g} + A_{1u} + A_{2g} + 2E_g + A_{2u} + 2E_u$
<b>Mode classifications</b>		
$\Gamma_{\text{Raman}} = 2A_{1g} + B_{1g} + B_{2g} + 3E_g$ , $\Gamma_{\text{IR}} = 3A_{2u} + 7E_u$ , $\Gamma_{\text{Acoustic}} = A_{2u} + E_u$		
$\Gamma_{\text{Mech}} = 2A_{1g} + 2A_{1u} + 2A_{2g} + 4A_{2u} + B_{1g} + 2B_{1u} + B_{2g} + 8E_u + 3E_g$		
<b>Raman tensor</b>		
$A_{1g} = \begin{bmatrix} a & 0 & 0 \\ 0 & a & 0 \\ 0 & 0 & b \end{bmatrix}$ $E_g = \begin{bmatrix} 0 & 0 & 0 \\ 0 & 0 & e \\ 0 & e & 0 \end{bmatrix}$ $E_g = \begin{bmatrix} 0 & 0 & -e \\ 0 & 0 & 0 \\ -e & 0 & 0 \end{bmatrix}$ $B_{1g} = \begin{bmatrix} c & 0 & 0 \\ 0 & -c & 0 \\ 0 & 0 & 0 \end{bmatrix}$ $B_{2g} = \begin{bmatrix} 0 & d & 0 \\ d & 0 & 0 \\ 0 & 0 & 0 \end{bmatrix}$		
<b><math>Pmmn</math> (59) <math>D_{2h}^{13}</math></b>		
Cs1	2a	$A_g + B_{2g} + B_{3g} + B_{1u} + B_{2u} + B_{3u}$
Cs2	2b	$A_g + B_{2g} + B_{3g} + B_{1u} + B_{2u} + B_{3u}$
Sc	4d	$3A_{1u} + 3B_{1u} + 3B_{2u} + 3B_{3u}$
F1	4e	$2A_g + B_{1g} + B_{2g} + 2B_{3g} + 2B_{1u} + 2B_{2u} + B_{3u} + A_u$
F2	4f	$2A_g + B_{1g} + 2B_{2g} + B_{3g} + 2B_{1u} + B_{2u} + 2B_{3u} + A_u$
F3	8g	$3A_g + 3B_{1g} + 3B_{2g} + 3B_{3g} + 3B_{1u} + 3B_{2u} + 3B_{3u} + 3A_u$
<b>Mode classifications</b>		
$\Gamma_{\text{Raman}} = 9A_g + 5B_{1g} + 8B_{2g} + 8B_{3g}$ , $\Gamma_{\text{IR}} = 11B_{1u} + 10B_{2u} + 10B_{3u}$ , $\Gamma_{\text{Acoustic}} = B_{1u} + B_{2u} + B_{3u}$		
$\Gamma_{\text{Mech}} = 9A_g + 8A_u + 5B_{1g} + 12B_{1u} + 8B_{2g} + 11B_{2u} + 8B_{3g} + 11B_{3u}$		
<b>Raman tensor</b>		
$A_{1g} = \begin{bmatrix} a & 0 & 0 \\ 0 & a & 0 \\ 0 & 0 & c \end{bmatrix}$ $B_{3g} = \begin{bmatrix} 0 & 0 & 0 \\ 0 & 0 & f \\ 0 & f & 0 \end{bmatrix}$ $B_{2g} = \begin{bmatrix} 0 & 0 & e \\ 0 & 0 & 0 \\ e & 0 & 0 \end{bmatrix}$ $B_{1g} = \begin{bmatrix} 0 & d & 0 \\ d & 0 & 0 \\ 0 & 0 & 0 \end{bmatrix}$		



**Table 6** Calculated and experimental IR wavenumbers

Symm. type	Calc. mode, cm <sup>-1</sup>	IR, (133 K) experiment, cm <sup>-1</sup>
<i>B</i> <sub>1u</sub>	8.0	
<i>B</i> <sub>2u</sub>	8.37	
<i>B</i> <sub>3u</sub>	8.8	
<i>B</i> <sub>1u</sub>	11.9	
<i>B</i> <sub>2u</sub>	12.1	
<i>B</i> <sub>3u</sub>	12.9	
<i>B</i> <sub>2u</sub>	82.96	
<i>B</i> <sub>3u</sub>	85.1	110
<i>B</i> <sub>1u</sub>	140.3	124
<i>B</i> <sub>3u</sub>	142.7	127
<i>B</i> <sub>1u</sub>	145.7	
<i>B</i> <sub>2u</sub>	146.5	
<i>B</i> <sub>2u</sub>	164.1	
<i>B</i> <sub>3u</sub>	165.6	
<i>B</i> <sub>1u</sub>	167.0	
<i>B</i> <sub>1u</sub>	168.1	
<i>B</i> <sub>3u</sub>	186.8	
<i>B</i> <sub>2u</sub>	188.9	
<i>B</i> <sub>1u</sub>	195.4	
<i>B</i> <sub>3u</sub>	203.3	
<i>B</i> <sub>2u</sub>	219.6	
<i>B</i> <sub>1u</sub>	223.1	223
<i>B</i> <sub>1u</sub>	270.9	249
<i>B</i> <sub>2u</sub>	272.9	
<i>B</i> <sub>3u</sub>	278.0	
<i>B</i> <sub>1u</sub>	280.0	392
<i>B</i> <sub>2u</sub>	503.4	436
<i>B</i> <sub>3u</sub>	524.7	487
<i>B</i> <sub>3u</sub>	609.1	
<i>B</i> <sub>2u</sub>	609.4	
<i>B</i> <sub>1u</sub>	610.1	587

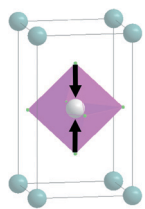
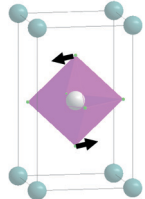
symmetry of the scandium position does not change and the distance to the nearest fluorine ions changes insignificantly, in the second coordination sphere, according to the X-ray results considerable changes occur which, in principle, should change the  $V_{zz}$  value. The absence of changes in the  $^{45}\text{Sc}$  NMR spectra indirectly proves the phase transition model ensuing from the Raman and X-ray data. The changes in the scandium spectrum related to very small structure variation should be very small.

In the low-temperature phase of  $\text{CsScF}_4$ , there are two structurally nonequivalent cesium atoms and, accordingly, two three-axis EFG tensors on the Cs nuclei. As a cesium NMR line from each structurally and magnetically nonequivalent position of cesium splits into 7 components, the quadrupole splitting is not more than 20 kHz, and the tensor parameters are quite close, the resolution in the spec-

**Table 7** Interatomic interaction potential parameters

Bond	$\lambda$ [aJ Å <sup>-1</sup> ]	$\rho$ [Å]
Cs–F	24.45810	0.333473
Sc–F1	199.2600	0.372764
Sc–F2	329.0828	0.384075
F1–F1	308.7130	0.378027
F1–F2	332.7137	0.384993
F2–F2	75.10116	0.349106

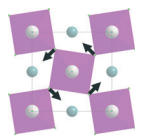
**Table 8** Symmetry type and vibration modes at 543 K in the  $P4/mmm$  phase

Symmetry type	Normal vibration modes	Calculated	Experimental
<i>A</i> <sub>1g</sub>		497	492
<i>E</i> <sub>g</sub>		155	155

trum is insufficient to accurately define parameters of the said tensors and the tilt angle of their principal axis  $V_{zz}$  from the  $c$  axis of the crystal. The phase transition into the intermediate phase ( $T_2 = 317$  K) is clearly recorded by considerable simplification of the  $^{133}\text{Cs}$  NMR spectra. Analysis of orientation dependences helps to find one axially symmetrical EFG tensor with a principal value of  $V_{zz} = 20$  kHz and the direction of the principal axis along the  $c$  axis. A further increase in temperature up to 510 K does not change the parameters of this tensor. The lack of changes in the cesium spectrum in the first phase transition (475 K) can be explained by the same reasons as in the scandium case, but here the situation is aggravated by much worse resolution associated with small quadrupole splitting.

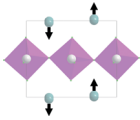
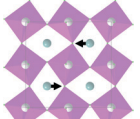
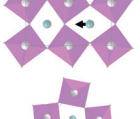

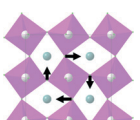
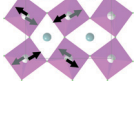

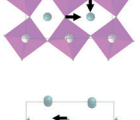

Thus, the NMR studies on the whole confirm the phase transition model developed on the basis of these Raman scattering and X-ray structural studies. However, it should be noted that the spectra of none of the nuclei under study exhibit the first phase transition at  $T = 475$  K. We assume this to be a consequence of specificity of structural changes taking place at this transition. An additional result is the exchange between equatorial and polar fluorine atoms found in

**Table 9** Symmetry type and vibration modes at 393 K in the  $P4/mbm$  phase

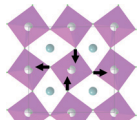
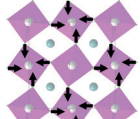
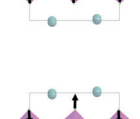
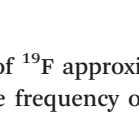
Symmetry type	Normal vibration modes	Calculated	Experimental
<i>E</i> <sub>g</sub>		33.6	
<i>A</i> <sub>1g</sub>		119	
<i>A</i> <sub>1g</sub>		109.1	
<i>E</i> <sub>g</sub>		154.9	
<i>E</i> <sub>g</sub>		253.9	
<i>B</i> <sub>2g</sub>		260.1	
<i>B</i> <sub>1g</sub>		451.5	
<i>A</i> <sub>1g</sub>		497.5	



**Table 10** Symmetry type and vibration modes at 193 K in the *Pmmn* phase

Symmetry type	Normal vibration modes	Calculated	Experimental
$A_g$		7.7	
$A_g$		8.2	
$B_{3g}$		8.4	
$B_{3g}$		8.6	
$B_{2g}$		8.9	
$B_{2g}$		9.1	
$A_g$		37.2	22.7
$B_{3g}$		46.0	
$A_g$		56.6	31.8
$B_{2g}$		65.2	63
$A_g$		91.5	121
$B_{1g}$		148.4	
$B_{2g}$		151.1	154.6
$B_{3g}$		152.3	157.7
$B_{1g}$		155.1	
$B_{2g}$		181.5	182
$B_{3g}$		183.8	
$A_g$		240.9	
$B_{3g}$		249.3	249.1
$A_g$		251.5	
$B_{2g}$		251.5	250.5
$A_g$		255.7	268.5

**Table 10 (continued)**

Symmetry type	Normal vibration modes	Calculated	Experimental
$B_{1g}$		438.6	
$B_{3g}$		443.5	
$B_{2g}$		448.0	
$B_{1g}$		449.3	452
$A_g$		489.3	497
$B_{3g}$		508.8	
$B_{2g}$		511.4	
$B_{1g}$		532.0	

NMR studies of  $^{19}\text{F}$  approximately 50 K above the first phase transition. The frequency of this exchange is found to be 20 kHz at 550 K and it increases with temperature.

## 6 Phase transition thermodynamic model

Critical one-dimensional IR of  $M2+$  induces changes in the crystal symmetry at the phase transition of the first order<sup>5,6</sup> and another phase transition of the second order is associated with OPs, transformed by two-dimensional IR of  $X2-$ . The free energy (FE) corresponding to these representations and describing phase transition sequences can be written as follows:

$$\begin{aligned}
 \Phi &= \Phi_M + \Phi_X + \Phi_{MX}, \\
 \Phi_M &= a_1 \eta^2 + a_2 \eta^4 + a_3 \eta^6, \\
 \Phi_M &= \alpha_1 I_1 + \alpha_2 I_1^2 + \beta_1 I_2 + \beta_2 I_2^2 + \delta I_1 I_2, \\
 \Phi_{MX} &= b \eta^2 I_1, \\
 I_1 &= \chi_1^2 + \chi_2^2 \\
 I_2 &= (\chi_1^2 + \chi_2^2)^2
 \end{aligned} \quad (11)$$

where  $\Phi_M$  is the part of the potential associated with  $M2+$ ,  $\Phi_X$  is the part of the potential associated with  $X2-$ ,  $\Phi_{MX}$  is the interaction potential, and  $\eta$ ,  $\chi_1$ , and  $\chi_2$  are the OP components. Below, we assume  $\delta = 0$ ; it was shown in ref. 47 that such an assumption should not significantly affect the results to be produced.

To describe phase transition of the first order,  $\Phi_M$  – part of the FE associated with one-dimensional IRs – is written up to the 6th power of the OP  $\eta$ . This ensues from the necessity of describing phase transition of the first order.<sup>46</sup> For the



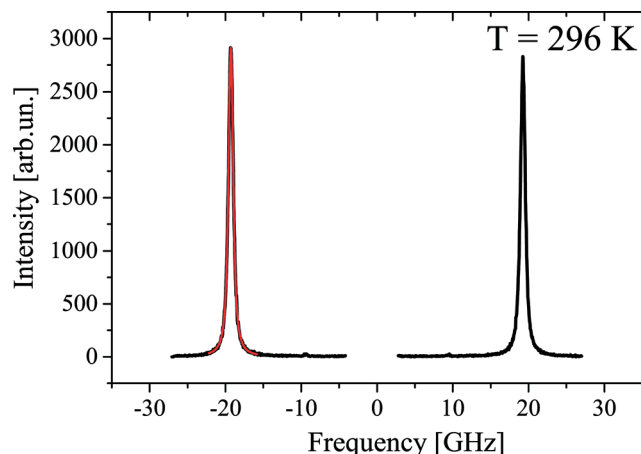


Fig. 11 CsScF<sub>4</sub> Brillouin scattering spectrum and fit at 296 K.

same reason, we assume  $a_2 < 0$ . The other  $-\Phi_X$  part of FE is written up to the 8th power of the two-component OP ( $\chi_1$ ,  $\chi_2$ ), as this is the lowest power at which the emergence of all low-symmetry phases occurring in the experiments can be described.<sup>5,6</sup>

Two more restrictions on the TP coefficients are imposed by the conditions of the existence of global minimum:  $a_3 > 0$  and  $a_5 > 0$ . A similar free energy but with expansion to the fourth power of  $\eta$  OP was considered in ref. 47. The given FE

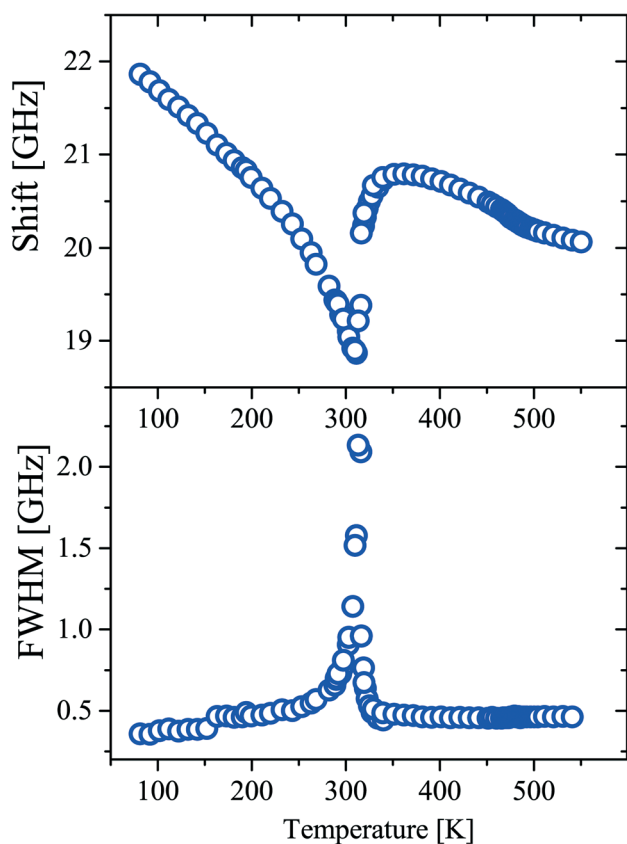


Fig. 12 Temperature dependencies of the position and width (FWHM) of the Brillouin component.

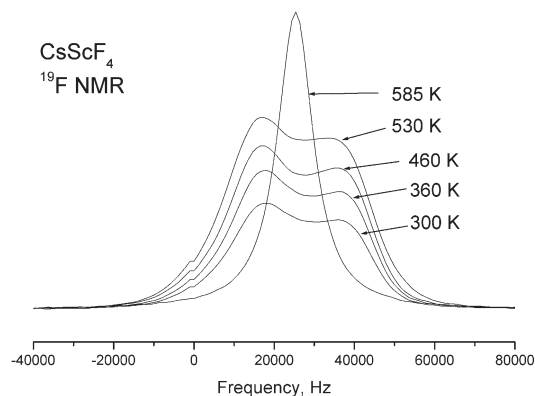


Fig. 13 Temperature evolution of the centroid of the <sup>19</sup>F spectrum line.

was analyzed and phase state diagrams were described in a standard manner similar to the one described in ref. 46. In the case of the CsScF<sub>4</sub> crystal, the transition temperatures are apart from each other by more than 100 degrees, so in eqn (11) we leave the first term of expansion only.

### 6.1 Possible types of phase diagrams

Fig. 15 and 16 show the obtained phase diagrams. First order phase transitions are shown by full lines and second order phase transitions by dashed ones; the dash-dotted lines are the boundaries of phase stability for the first order transitions. Thin full lines numbered 1 and 2 depict a thermodynamic path realized in the CsScF<sub>4</sub> crystal. The temperatures of the observed phase transitions differ considerably, so the coefficient  $b$  from  $\Phi_{MX}$  should be nonzero and its sign determines the succession of transitions: for positive  $b$ , the first transition occurs in the phase with nonzero  $\eta$ , *i.e.* phase  $(\eta, 0, 0)$ . Negative  $b$  results in the phase  $(0, \chi, \chi)$ . The phase diagrams produced are shifted along  $a_1$  and  $\alpha_1$  against the diagrams for non-interacting OP  $\eta$  and  $\chi$  by the value proportional to coefficient  $b$ . It is possible to transit from phase  $(\eta, 0, 0)$  into  $(\eta, \chi, \chi)$  only when  $\beta_1 > 0$ . For negative  $\beta_1$ , phase  $(\eta, 0, 0)$  transits into phase  $(\eta, \chi, 0)$ . A more detailed examination

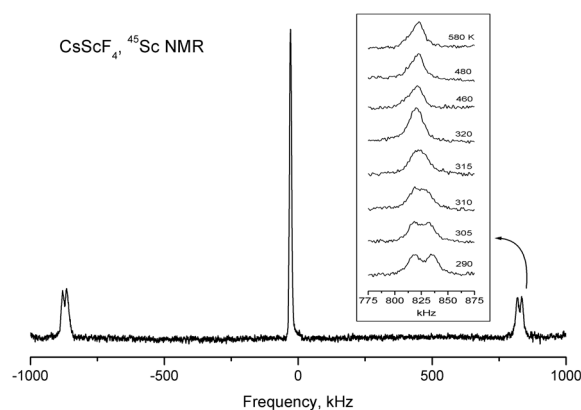


Fig. 14 Temperature evolution of <sup>45</sup>Sc NMR spectrum lines.





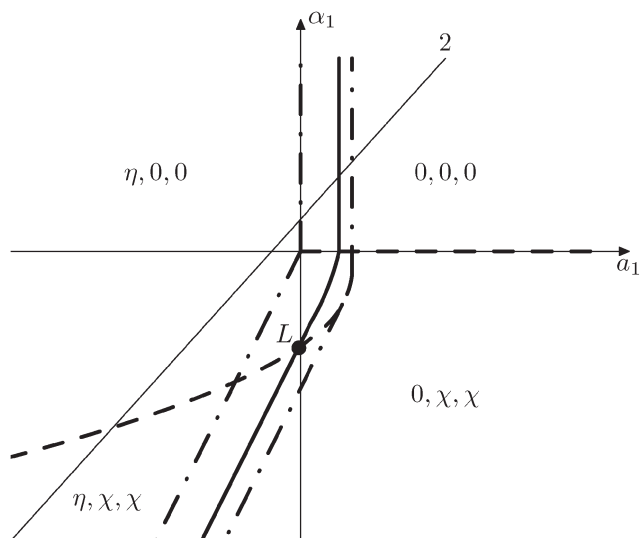


Fig. 15 Diagram of the phase state of the thermodynamic potential at  $a_2 < 0$ ,  $\beta_2 > 0$ ,  $b > 0$ . The first order transition is denoted as a solid line, the second order transition as a dashed line, and the bucking phases as a dash-dotted line.

of the diagram in Fig. 16 shows that the boundary (full line in Fig. 16) of the first order phase transition between phases  $(\eta, 0, 0)$  and  $(0, \chi, \chi)$  runs along the line

$$\alpha_1 = \frac{2}{3a_3\sqrt{3}} \sqrt{-\alpha_2 \left[ 2(a_2 - \sqrt{a_2^2 - 3a_1a_3})(a_2^2 - 3a_1a_3) - 3a_1a_2a_3 \right]}$$

The stability zone of the phase with OP  $(0, \chi, \chi)$  is restricted by the dash-dotted straight line from the origin of the coordinates in Fig. 16. Phases  $(\eta, 0, 0)$  and  $(\eta, \chi, \chi)$  are separated by the line of the second order transition  $a_1 = \alpha_1(2ba_2 - 3\alpha_1a_3)/b^2$  (dashed line). Contrary to ref. 47, the

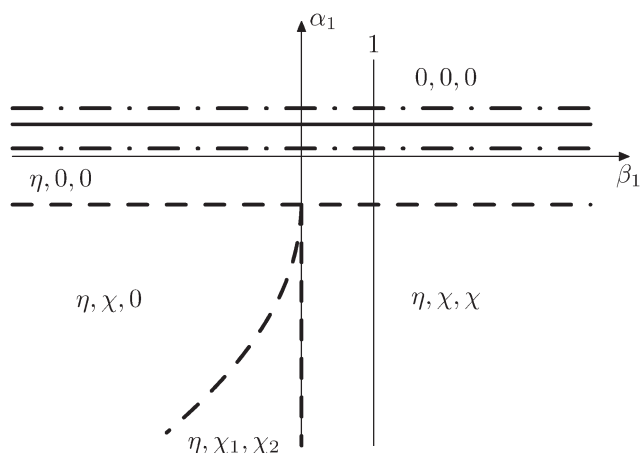


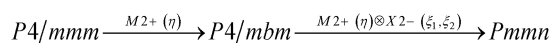
Fig. 16 Diagram of the phase state of the thermodynamic potential at  $a_2 < 0$ ,  $\beta_2 > 0$ ,  $\beta_1 > 0$ . The full line denotes the first order transition, the dashed line denotes the second order transition, and the dash-dotted line denotes the bucking phases.

boundary of phase  $(\eta, 0, 0)$  is described by a quadratic equation.  $a_1 = \frac{-(b^2 - 4a_2\alpha_2)(4a_2\alpha_2 + 3b^2)}{64\alpha_2^2a_3}$ ;  $a_1 = \frac{-b(-4a_2\alpha_2 + b^2)}{8a_2a_3}$ . At

the phase diagram, there exist a point  $L$  with the coordinates  $(\eta, 0, 0)$ ,  $(\eta, \chi, \chi)$  and  $(0, \chi, \chi)$  where three phases coexist.

## 7 Conclusions

We have found relationships between the coefficients of thermodynamic potential as a function of order parameters of one-dimensional  $M2+$  and two-dimensional  $X2-$  irreducible representations which can occur in layered perovskite  $\text{CsScF}_4$ . Expressions for phase boundaries have been accurately derived from the considered potential. Knowing the pattern of phase states, one can conceive how it changes under external influence of different kind which is necessary for a conscious choice of crystals and understanding possible impacts on them in some applications. The sequence of phase transitions has been reinvestigated:



At the first phase transition,  $\text{ScF}_6$  octahedra rotate jumpwise by  $\phi \sim \eta$  that accounts for the first order transition. There are no other rotations or heavy atom displacements. At the second phase transition, two new rotations appeared: around the  $\bar{a} + \bar{b}$  axis on angle  $\psi_1 \sim \xi_1$  and around the  $\bar{a} - \bar{b}$  axis on angle  $\psi_2 \sim \xi_2$ . Cs1 and Cs2 atoms move along the  $c$  axis at this second transition. The mechanisms of all phase transitions are of displacive distortion type. The results of vibrational spectroscopy and NMR studies all in all confirm this phase transition model developed on the basis of the XRD data and thermodynamic model.

## Acknowledgements

The authors are grateful to Prof. I. N. Flerov for valuable support and useful discussions. This work was partly supported by the Russian Foundation for Basic Research, Project 16-02-00102. The research is partially conducted within the framework of the state task of the Ministry of Education and Science of the Russian Federation for Siberian Federal University on R&D performance in 2014 (Task 3.2534.2014/K). X-ray data from powders, Raman NMR, and IR spectra were obtained with use the analytical equipment of Krasnoyarsk Center of collective use SB RAS.

## References

- 1 K. S. Aleksandrov and J. Bartolome, *Phase Transitions*, 2001, 74, 255–336.
- 2 S. S. P. Parkin, V. Y. Lee, A. I. Nazzari, R. Savoy, R. Beyers and S. J. LaPlaca, *Phys. Rev. Lett.*, 1988, 61, 750–753.
- 3 H. Arend, W. Huber, F. H. Mischgovsky and G. Richter, *J. Cryst. Growth*, 1978, 43, 213–223.



- 4 K. S. Aleksandrov and B. V. Beznosikov, *Perovskites: Present and Future. Variety of Parent Phases, Phase Transitions, Possibilities of Synthesis of New Compounds*, SB RAS, Novosibirsk, 2004.
- 5 K. S. Aleksandrov, B. V. Beznosikov and S. V. Misyul, *Ferroelectrics*, 1987, 73, 201–211.
- 6 I. N. Flerov, K. S. Aleksandrov, S. V. Melnikova, A. I. Kruglik, S. V. Misjul and B. V. Beznosikov, *Ferroelectrics*, 1989, 96, 175–179.
- 7 A. Bulou, M. Debiéche, J. Nouet, F. Ganot, C. Dugautier and P. Moch, *Phase Transitions*, 1991, 33, 99.
- 8 F. Ganot, M. Papin, A. Bulou and P. Moch, *Ferroelectrics*, 1991, 124, 321.
- 9 M. Papin, A. Bulou and J. Nouet, *J. Phys.: Condens. Matter*, 1993, 87, 232.
- 10 M. Couzi, P. L. Loyzance, R. Mokhlisse, A. Bulou and J. L. Fourquet, *Phys. Chem. Chem. Phys.*, 1983, 87, 232.
- 11 Q. Wang, G. Ripault and A. Bulou, *Phase Transitions*, 1995, 53, 1.
- 12 Q. Wang, A. Bulou and A. Desert, *J. Phys.: Condens. Matter*, 1995, 7, 825.
- 13 A. Bulou and J. Nouet, *J. Phys. C: Solid State Phys.*, 1987, 20, 2885.
- 14 A. Bulou, M. Rousseau and B. Hennion, *J. Phys.: Condens. Matter*, 1989, 1, 4553.
- 15 E. Palacios-Lidón, E. Palacios, R. Burriel and A. Bulou, *Ferroelectrics*, 2002, 270, 387.
- 16 B. K. Greve, K. L. Martin, P. L. Lee, P. J. Chupas, K. W. Chapman and A. P. Wilkinson, *J. Am. Chem. Soc.*, 2010, 132, 15496.
- 17 C. W. Li, X. Tang, J. A. Munoz, J. B. Keith, S. J. Tracy, D. L. Abernathy and B. Fultz, *Phys. Rev. Lett.*, 2011, 107, 195504.
- 18 L. Hu, J. Chen, L. Fan, J. Deng, R. Yu and X. Xing, *J. Am. Ceram. Soc.*, 2014, 97, 1009.
- 19 O. V. Kovalev, *Irreducible Representations of the Space Groups*, Routledge, 1965.
- 20 S. C. Miller and W. F. Love, *Tables of Irreducible Representations of The Space Groups and Co-Representations of Magnetic Space Groups*, Pruett Press Boulder, Colorado, 1967.
- 21 V. P. Sakhnenko, V. M. Talanov and G. M. Chechin, *Fiz. Met. Metalloved.*, 1986, 62, 847–856.
- 22 A. N. Vtyurin, A. S. Krylov, I. V. Shmygol and A. P. Shebanin, *Phys. Solid State*, 1997, 39, 632–633.
- 23 I. C. Madsen and R. J. Hill, *Adv. X-Ray Anal.*, 1992, 35, 39–47.
- 24 I. C. Madsen and R. J. Hill, *J. Appl. Crystallogr.*, 1994, 27, 385–392.
- 25 W. I. F. David, *Abstract P2.6, NIST Special Publication*, 1992, vol. 846, p. 210.
- 26 *DiffraC-Plus Basic XRD Wizard*, Bruker AXS GmbH, Karlsruhe, Germany, 2002–2007.
- 27 A. S. Krylov, E. M. Merkusheva, A. N. Vtyurin and L. I. Isaenko, *Phys. Solid State*, 2012, 54, 1275.
- 28 A. S. Krylov, E. M. Kolesnikova, L. I. Isaenko, S. N. Krylova and A. N. Vtyurin, *Cryst. Growth Des.*, 2014, 14, 923.
- 29 S. M. Lindsay, M. W. Anderson and J. R. Sandercock, *Rev. Sci. Instrum.*, 1981, 52, 1478.
- 30 H. T. Stokes, D. M. Hatch and B. J. Campbell, *ISOTROPY*, 2007, stokes.byu.edu/isotropy.html.
- 31 B. J. Campbell, H. T. Stokes, D. E. Tanner and D. M. Hatch, *J. Appl. Crystallogr.*, 2006, 39, 607.
- 32 A. N. Vtyurin, A. Bulou, A. S. Krylov, I. V. Shmygol and K. S. Aleksandrov, *J. Raman Spectrosc.*, 2000, 31, 151–155.
- 33 A. S. Krylov, I. V. Shmygol, A. P. Shebanin, A. N. Vtyurin and A. G. Ageev, *Ferroelectrics*, 1999, 233, 103.
- 34 I. N. Flerov, M. V. Gorev, J. Grannec and A. Tressaud, *J. Fluorine Chem.*, 2002, 116, 9–14.
- 35 L. H. Hoang, N. T. M. Hien, W. S. Choi, Y. S. Lee, K. Taniguchi, T. Arima, S. Yoon, X. B. Chen and I.-S. Yang, *J. Raman Spectrosc.*, 2010, 41, 1005.
- 36 V. K. Malinovsky, A. M. Pugachev and N. V. Surovtsev, *Phys. Solid State*, 2008, 50, 1137.
- 37 M. B. Smirnov and V. Yu. Kazimirov, *LADY: software for lattice dynamics simulations*, JINR communications, E 14-2001-159, 2001.
- 38 M. B. Smirnov, A. P. Mirgorodsky and P. E. Quintard, *J. Mol. Struct.*, 1995, 348, 159.
- 39 A. A. Savina, V. V. Atuchin, S. F. Solodovnikov, Z. A. Solodovnikova, A. S. Krylov, E. A. Maximovskiy, M. S. Molokeev, A. S. Oreshonkov, A. M. Pugachev and E. G. Khaikina, *J. Solid State Chem.*, 2015, 225, 53–58.
- 40 A. N. Vtyurin, A. S. Krylov, S. N. Krylova, S. V. Goryainov, V. N. Voronov and A. S. Oreshonkov, *Ferroelectrics*, 2012, 440, 100–104.
- 41 A. N. Vtyurin, A. S. Krylov, S. V. Goryainov, S. N. Krylova, A. S. Oreshonkov and V. N. Voronov, *Phys. Solid State*, 2012, 54, 934–936.
- 42 A. S. Krylov, A. N. Vtyurin, A. S. Oreshonkov, V. N. Voronov and S. N. Krylova, *J. Raman Spectrosc.*, 2013, 44, 763–769.
- 43 Yu. V. Gerasimova, A. S. Oreshonkov, A. N. Vtyurin, A. A. Ivanenko, L. I. Isaenko, A. A. Ershov and E. I. Pogoreltsev, *Phys. Solid State*, 2013, 55, 2331–2334.
- 44 Xia Zhiguo, M. S. Molokeev, A. S. Oreshonkov, V. V. Atuchin, R.-S. Liu and C. Dong, *Phys. Chem. Chem. Phys.*, 2014, 16, 5952–5957.
- 45 V. V. Atuchin, A. S. Aleksandrovsky, O. D. Chimitova, T. A. Gavrilova, A. S. Krylov, M. S. Molokeev, A. S. Oreshonkov, B. G. Bazarov and J. G. Bazarova, *J. Phys. Chem. C*, 2014, 118, 15404–15411.
- 46 Y. A. Izyumov and V. N. Syromyatnikov, *Phase Transitions and Crystal Symmetry*, Springer Netherlands, 1990, p. 444.
- 47 M. P. Ivliev and V. P. Sakhnenko, *Ferroelectrics*, 1996, 175, 65–71.

